Laboratory observations of permeability enhancement by fluid pressure oscillation of in situ fractured rock

Jean E. Elkhoury,[1,2] André Niemeijer,[3,4] Emily E. Brodsky,[1] and Chris Marone[3]

Received 5 June 2010; revised 5 November 2010; accepted 22 December 2010; published 24 February 2011.

[1] We report on laboratory experiments designed to investigate the influence of pore pressure oscillations on the effective permeability of fractured rock. Berea sandstone samples were fractured in situ under triaxial stresses of tens of megapascals, and deionized water was forced through the incipient fracture under conditions of steady and oscillating pore pressure. We find that short-term pore pressure oscillations induce long-term transient increases in effective permeability of the fractured samples. The magnitude of the effective permeability enhancements scales with the amplitude of pore pressure oscillations, and changes persist well after the stress perturbation. The maximum value of effective permeability enhancement is 5×10^{-16} m^2 with a background permeability of 1×10^{-15} m^2; that is, the maximum enhanced permeability is 1.5×10^{-15} m^2. We evaluate poroelastic effects and show that hydraulic storage release does not explain our observations. Effective permeability recovery following dynamic oscillations occurs as the inverse square root of time. The recovery indicates that a reversible mechanism, such as clogging/unclogging of fractures, as opposed to an irreversible one, like microfracturing, is responsible for the transient effective permeability increase. Our work suggests the feasibility of dynamically controlling the effective permeability of fractured systems. The result has consequences for models of earthquake triggering and permeability enhancement in fault zones due to dynamic shaking from near and distant earthquakes.

Citation: Elkhoury, J. E., A. Niemeijer, E. E. Brodsky, and C. Marone (2011), Laboratory observations of permeability enhancement by fluid pressure oscillation of in situ fractured rock, *J. Geophys. Res.*, *116*, B02311, doi:10.1029/2010JB007759.

1. Introduction

[2] Fluid flow in Earth's crust shows a strong sensitivity to dynamic stressing [e.g., *Manga and Wang*, 2007]. The passage of seismic waves can increase both the frequency of geyser eruptions and the local rates of stream flows [*Rojstaczer and Wolf*, 1992; *Muir-Wood and King*, 1993; *Manga and Brodsky*, 2006; *Manga et al.*, 2003; *Manga and Wang* 2007]. Seismic waves can also temporarily enhance oil production and spring discharge [*Beresnev and Johnson*, 1994; *Roberts et al.*, 2003; *Manga et al.*, 2003]. Dynamic stresses associated with the passage of seismic waves have also been observed to cause transient changes in water well levels [*Coble*, 1965; *Brodsky et al.*, 2003; *Elkhoury et al.*, 2006].

[3] These observed flow phenomena have been suggested to result from transient changes in local permeability due to dynamic shaking [*Manga et al.*, 2003; *Manga and Brodsky*, 2006; *Elkhoury et al.*, 2006; *Doan et al.*, 2007]. Dynamic stresses in the elastic waves can produce large oscillations in pore pressure that appear to drive these permeability changes [*Brodsky et al.*, 2003]. In addition, dynamic stresses produced by the passage of seismic waves can trigger seismicity, tremors, and other modes of fault slip, even at great distances from the main shock [e.g., *Hill et al.*, 1993; *Felzer and Brodsky*, 2006; *Manga and Wang*, 2007; *Rubinstein et al.*, 2007; *Gomberg et al.*, 2008; *Shelly*, 2010]. One explanation for these triggered slip events involves transient changes in fluid pressure due to flow resulting from permeability enhancement in the fault zone [*Brodsky et al.*, 2003]. However, the mechanism of the permeability increase from dynamic stressing is not well understood for either the flow phenomena or the seismic observations. The purpose of our study is to investigate the effect of dynamic stressing on the effective permeability of fractured rock in order to improve the understanding of these observations.

[4] In this study, we address the mechanisms of permeability enhancement by dynamic stressing using controlled laboratory tests. We produced fractures under true triaxial stresses with fully saturated conditions and then applied sinusoidal oscillations in the upstream pore pressure while holding the downstream pore pressure and the applied stresses on the sample boundaries constant. We measured the permeability of the sample, via fluid flow, continuously during the experiment and found that the permeability after

[1]Department of Earth and Planetary Sciences, University of California, Santa Cruz, California, USA.
[2]Now at Seismological Laboratory, California Institute of Technology, Pasadena, California, USA.
[3]Department of Geosciences, Pennsylvania State University, University Park, Pennsylvania, USA.
[4]Now at Istituto Nazionale di Geofisica e Vulcanologia, Rome, Italy.

0148-0227/11/2010JB007759

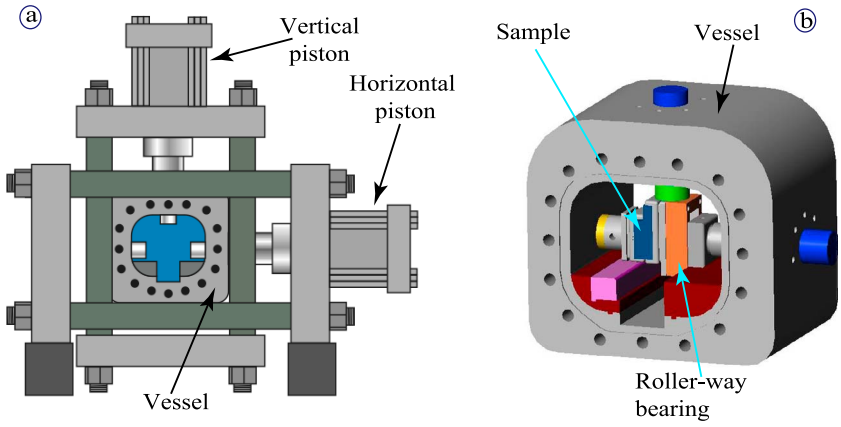

Figure 1. Schematic of the testing apparatus. (a) Loading frame showing horizontal and vertical pistons, which provide normal and shear stresses on the eventual fracture plane, and pressure vessel where confining fluid pressure provides the third stress component. (b) Detail of pressure vessel showing L-shaped rock sample (blue). The single direct shear configuration is used with a frictionless roller-way bearing (orange) to fracture the sample in direct shear under applied load normal to the candidate fracture plane.

the pressure oscillations increased systematically with increasing amplitude of the oscillations.

[5] This paper begins with a description of the experimental procedure and laboratory results. We then translate the flow measurements to permeability while addressing poroelastic effects, boundary conditions of the applied loads, and issues of fluid flow in porous media such as specific storage. We interpret the resulting permeability enhancements by examining both the repeatability of the permeability recovery and the functional form of the relationship between transient pore pressure amplitude and permeability increase. Finally, we discuss possible applications of the results to field conditions applicable to reservoir engineering and earthquake physics.

2. Experimental Procedure

[6] The goal of our experiments was to measure the permeability response of fractured rock to dynamic stresses created by fluid pressure oscillations. The experimental procedure consists of two stages. In the first stage, we fractured intact samples within the testing apparatus while flowing fluid through the samples under controlled boundary conditions (Figure 1). Once the fluid flow through the fractured sample reached steady state, and flow rates at the inlet and outlet were the same, we investigated the role of dynamic stressing on effective permeability of the samples in the second stage of the experiment by oscillating the upstream pore fluid pressure. We measured fluid flow rates independently at both the inlet and outlet of the sample (Figure 2), and all stresses, strains, fluid pressures and fluid volumes were measured continuously throughout the experiment. Digital data were collected with a 24-bit A/D system recording at a rate of 10 kHz and averaged to rates of 10 Hz. The testing apparatus consists of a pressure vessel within a biaxial load frame (Figure 1). A true triaxial stress state is achieved via two loads applied through the pistons and the confining pressure. Each stress is controlled independently via a fast acting servo controller (for details of the apparatus, see *Samuelson et al.* [2009] and *Ikari et al.* [2009]).

[7] Each experiment started with an intact, presaturated, sample of Berea sandstone. We chose Berea sandstone because (1) it is homogeneous, which allows reproducible results on multiple samples, (2) it is considered a representative reservoir rock and its properties are well characterized [e.g., *Wang*, 2000], and (3) it has a relatively high permeability that is important in ensuring reasonable durations of the experiments.

[8] Samples of Berea were cut into L-shaped blocks that are roughly 3 × 4 × 7 cm in dimension (Figure 3a). The blocks were jacketed in a latex membrane and placed in the direct shear configuration (Figure 3b). Horizontal and vertical pistons together with a confining pressure loaded the sample. For all experiments, the normal stress across the eventual fracture plane was held at 23 MPa and the confining stress was set to 9 MPa, so that the effective normal stress was between 19 and 21 MPa, depending on the applied pore pressure (Table 1). These values were maintained constant during the entire experiment via servo control.

[9] The next step in our experiments was to initialize the flow system (Figure 3c). We implemented a pore pressure gradient by applying fluid pressure to the inlet and flushing the system until clear fluid (deionized water) flowed from the outlet. We then connected the second (outlet) pore pressure intensifier, bled trapped air, and applied a controlled pressure differential, ΔP, until the flow rate reached steady state (i.e., equal flow rates at the inlet and the outlet). Pore pressures were servo-controlled independently and applied via line sources at the inlet and outlet (Figures 2 and 3b). The fluid inlet and outlet consisted of a narrow channel fed by 3 holes (Figure 2). The channel was covered with 30 μm nylon filter paper to avoid clogging.

[10] We measured inlet and outlet flow volumes, to a resolution of 5.1×10^{-5} cm^3, via linear variable differential transformers (LVDTs) mounted on the intensifier pistons. The mean value of the pore pressure, Pp, was ~3.0 MPa with pressure differential, ΔP, of ~0.3 MPa (Table 1). The amplitude, A, of the Pp oscillation ranged from 0.02 to 0.3 MPa. We applied multiple sets of oscillations during a given experiment (Figure 4).

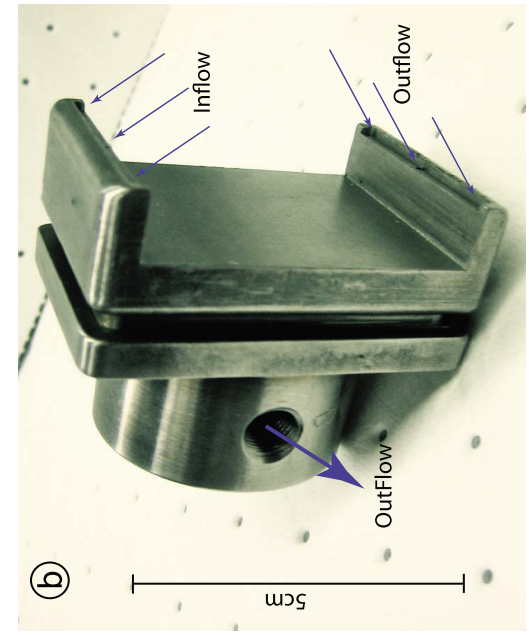

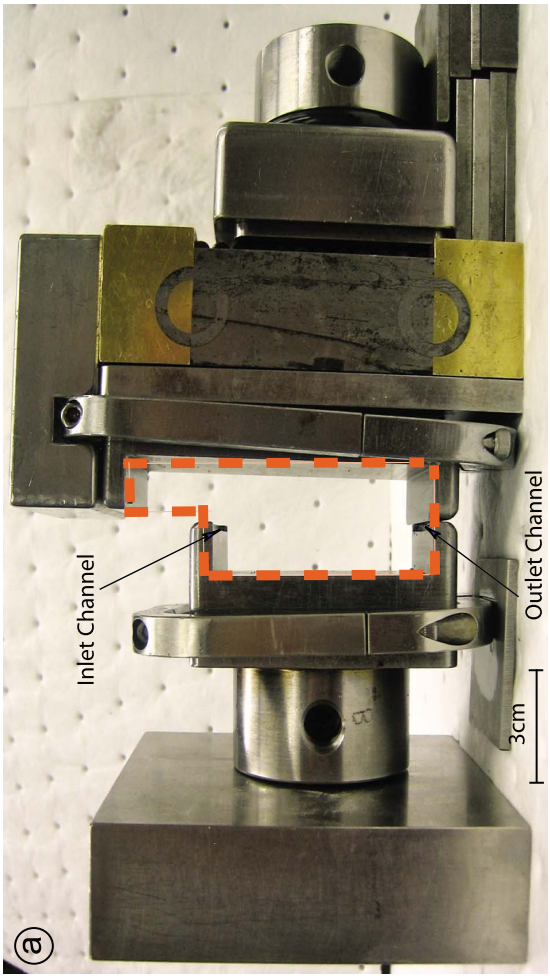

Figure 2. Sample configuration with main components arranged on a bench top (note that the sample jacket and load support blocks are not shown and that alignment is not complete). (a) Orange dashed line highlights the sample location. A latex jacket covers the sample during an experiment (see Figure 3b). (b) Enlargement of the sample loading platen (left side of Figure 3a) shown without the jacket sealing collar. Fluid ports and internal conduits in the platen provide flow through the rock sample. Pore pressures are servo-controlled and applied via line sources at the inlet and outlet, which consisted of a narrow channel fed by three holes. The channel was covered with 30 μm nylon filter paper to avoid clogging. Inflow port (at the back of the platen) is not seen in this photo.

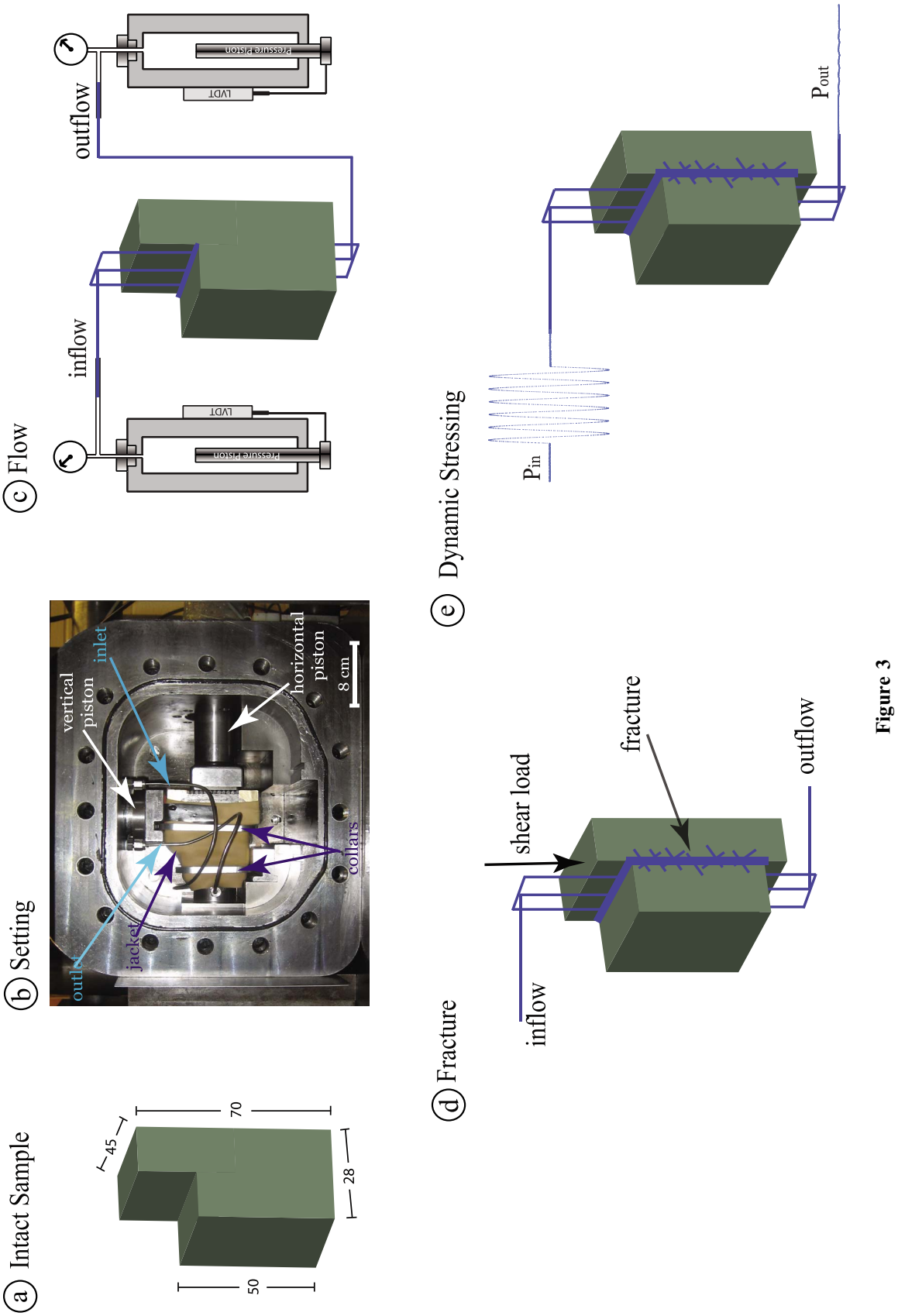
a Intact Sample
45
70
28
50
b Setting
vertical piston
inlet
horizontal piston
8 cm
outlet
jacket
collars
c Flow
outflow
inflow
LVDT
Pressure Piston
d Fracture
shear load
fracture
outflow
inflow
e Dynamic Stressing
Pout
Pin

Figure 3

Table 1. Summary of Parameters for the Main Suite of Experiments, Including Experiment Number, Stress Conditions, Sample Dimensions, and Hydraulic Properties[a]

Parameters	p1605	p1819	p1820	p1830
Failure shear stress (MPa)	32	31	31	32
Residual shear stress (MPa)	17	16	17	15
Inlet pore pressure (MPa)	3.0	3.1	3.2	3.0
Outlet pore pressure (MPa)	2.8	2.8	2.8	2.7
Peak pressure amplitude (MPa)	0.02–0.18	0.03–0.25	0.05–0.28	0.05–0.28
Shear offset (mm)	0.6	1.0	1.3	0.7
Intact sample permeability ($\times 10^{-15}$ m^2)	2.5	2.4	2.3	2.8
k_{ref} (10^{-16} m^2)	10.0	1.0	1.0	1.0
Flow length L (mm)	49.4	49.7	49.8	49.9
Flow cross section S (10^{-3} m^2)	1.28	1.27	1.28	1.28

[a]Viscosity of water, $\mu = 8.89 \times 10^{-4}$ Pa s, is used in equation (1).

[11] Permeability was inferred via Darcy's law

$$k = \frac{\mu L}{S}\frac{Q}{\Delta P} \quad (1)$$

where k is the effective permeability [e.g., *Main et al.*, 2000] of the fractured sample, μ is viscosity of water, L is flow path, S is the cross section of the sample and the nominal area of the eventual fracture plane, Q is the flow rate, and ΔP is the pressure difference across the fracture. As long as the flow rates at the inlet and outlet of our sample are equal, the measured changes in flow rate represent changes in effective permeability because ΔP, sample volume, and water viscosity (i.e., temperature), remained constant. In the data presented below, we always verified that inlet and outlet flow were equal within the measurement resolution.

[12] We began to fracture the sample after it was subject to the nominal triaxial stress state detailed above and after pore fluid flow had reached steady state. Control experiments were also completed in which we applied pore fluid pressure oscillations to the intact sample, and these are presented below. Shear load was applied by advancing the vertical piston in servo displacement control at 5 μm/s, which increased stress on the top of the L-shaped block (Figure 3d). Figure 5 shows details of a representative experiment, with shear stress and permeability plotted as a function of the load point displacement during fracture development. The permeability values shown in Figure 5 are derived from the average flow rate computed at the inlet and outlet. We use measurements of the force applied at the top of the sample to compute shear stress on the eventual fracture plane, which has a nominal area of 2.2×10^{-3} m^2. Permeability is approximately constant until a small stress drop at a shear stress of ~20 MPa and then begins to increase with further loading. Significant inelastic yielding begins at a displacement of ~9.2 mm, and permeability shows a sharp increase at that point. The sample fractured at a shear stress of 32 MPa, which was a consistent observation for each experiment (Table 1). A loud acoustic emission and a sudden drop in stress accompanied the mode-II-dominated fracture (Figure 5c). These were also consistent observations for each of our experiments.

[13] Figure 5b shows a zoomed view of the shear stress and flow rates for the region around failure. The inlet and outlet flow rates track one another exactly prior to a displacement of 9.8 mm, but after this point there is clear departure, with the inlet showing higher flow rate. The difference in flow rate is consistent with microfracture and eventual brittle failure, which increases the pore volume of the sample. Figure 5 clearly shows that (1) the storage of the Berea sandstones increases with fracturing and (2) we can measure storage effects with fidelity should they occur. Comparison of the inlet and outlet flow rates in the vicinity of the fracture provides a sensitive measure of fracture development and indicates clear, transient changes in poromechanical storage of the sample. We discuss storage effects related to transient oscillations of pore pressure more fully below, but for now we simply note that our experiment protocol and testing apparatus are capable of resolving both subtle and significant changes in storage, effective sample permeability, fracture development, and strength.

[14] After fracturing of the sample, we stopped loading and maintained a constant position of the vertical ram. This point occurs at a displacement of 10.4 mm in Figure 5. This concluded the preparatory or first stage of the experiments. At this point we waited until steady state flow (i.e., constant permeability) was reestablished before proceeding, and then commenced dynamic pore pressure oscillations (Figure 3e).

[15] We imposed sinusoidal pore pressure oscillations of varying amplitude while maintaining constant period and duration (20 s and 120 s, respectively). In order to isolate the

Figure 3. Schematic of the experimental sequence. (a) Experiments started with an intact sample. Dimensions are in millimeters. The area S given in Table 1 is defined by the sample width and thickness, 28 mm and 45 mm. (b) Photo of pressure vessel with door removed showing the sample (within jacket), internal fluid pipes, and loading configuration. Fluid lines are connected to servo-controlled intensifiers (Figure 3c) through high-pressure fittings in the vessel wall. (c) Schematic diagram of the fluid pressure system. Pressure intensifiers are servo-controlled and can apply flow rate or fluid pressure boundary conditions at the top and bottom of the eventual fracture plane. (d) Fractured sample with fluid flow. The stress normal to the fracture plane was applied as a constant force boundary condition at the edge of the rock sample. Shear load along the fracture was applied as a displacement boundary condition at the top of the sample. (e) Once fluid flow from the inlet to the outlet had reached steady state flow, pore pressure oscillations were applied at the inlet while keeping outlet pressure constant. We observe changes in steady state flow rate before and after fluid pressure oscillations.

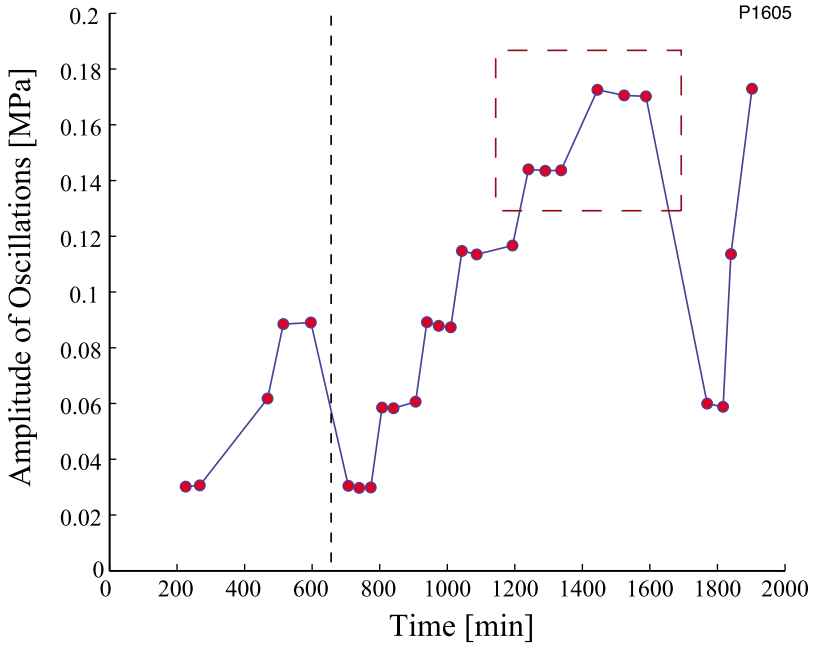

Figure 4. Time sequence of the applied pore pressure oscillations in a complete experiment (p1605). Each point represents a set of oscillations with 20 s period and 120 s duration. Intervals between oscillations sets were 30 to 100 min. Here, time = 0 corresponds to sample fracture. Dashed vertical line shows when fracture was sheared for 600 μm at a rate of 5 μm/s (see Figure 11). Boxed region denotes data shown in Figure 10.

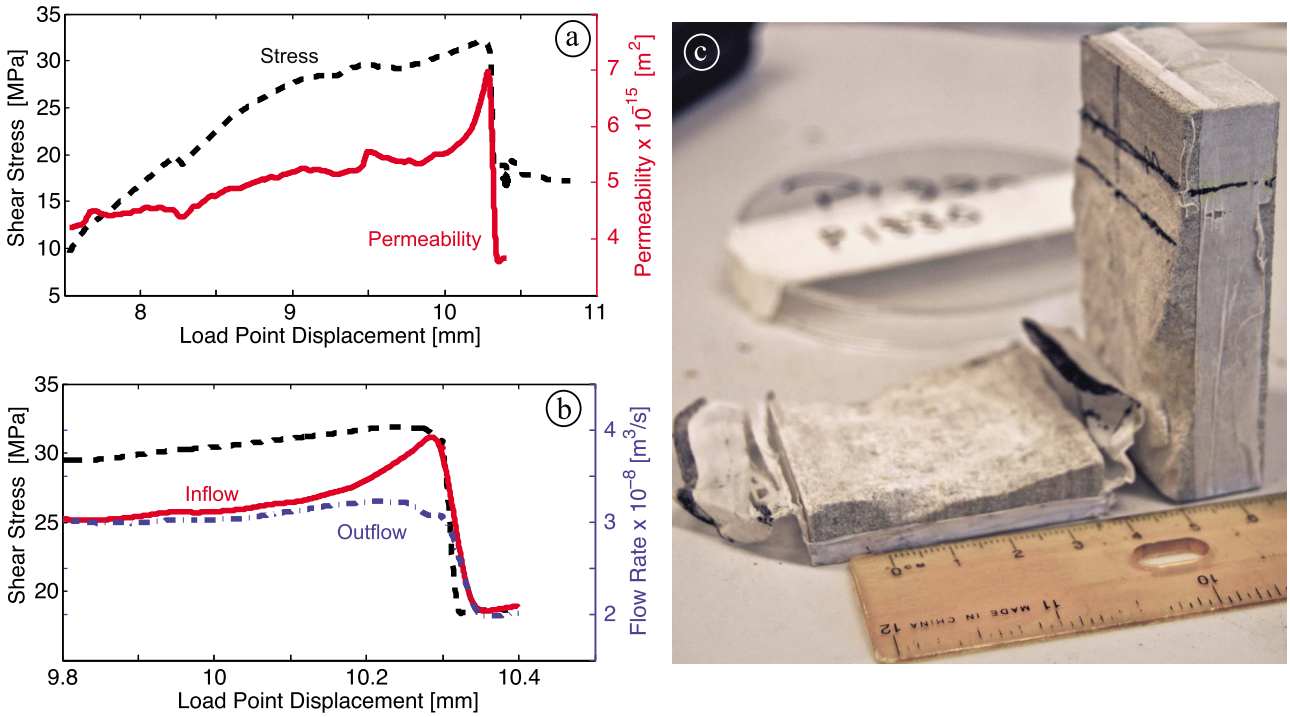

Figure 5. Fracture of the intact sample. (a) Strength and effective permeability are shown as a function of loading displacement during fracturing. Note that permeability increases slowly as stress rises to failure, and then permeability decreases dramatically. The permeability value is computed from the average inlet and outlet flow rates. (b) Comparison of strength data and flow rates measured at the inlet and outlet (see Figure 2 for flow geometry). Note that as the failure stress is approached, inlet flow exceeds outlet flow, indicating changes in porosity and specific storage. (c) Photograph of a fractured sample. The fracture is rough and predominantly mode II.

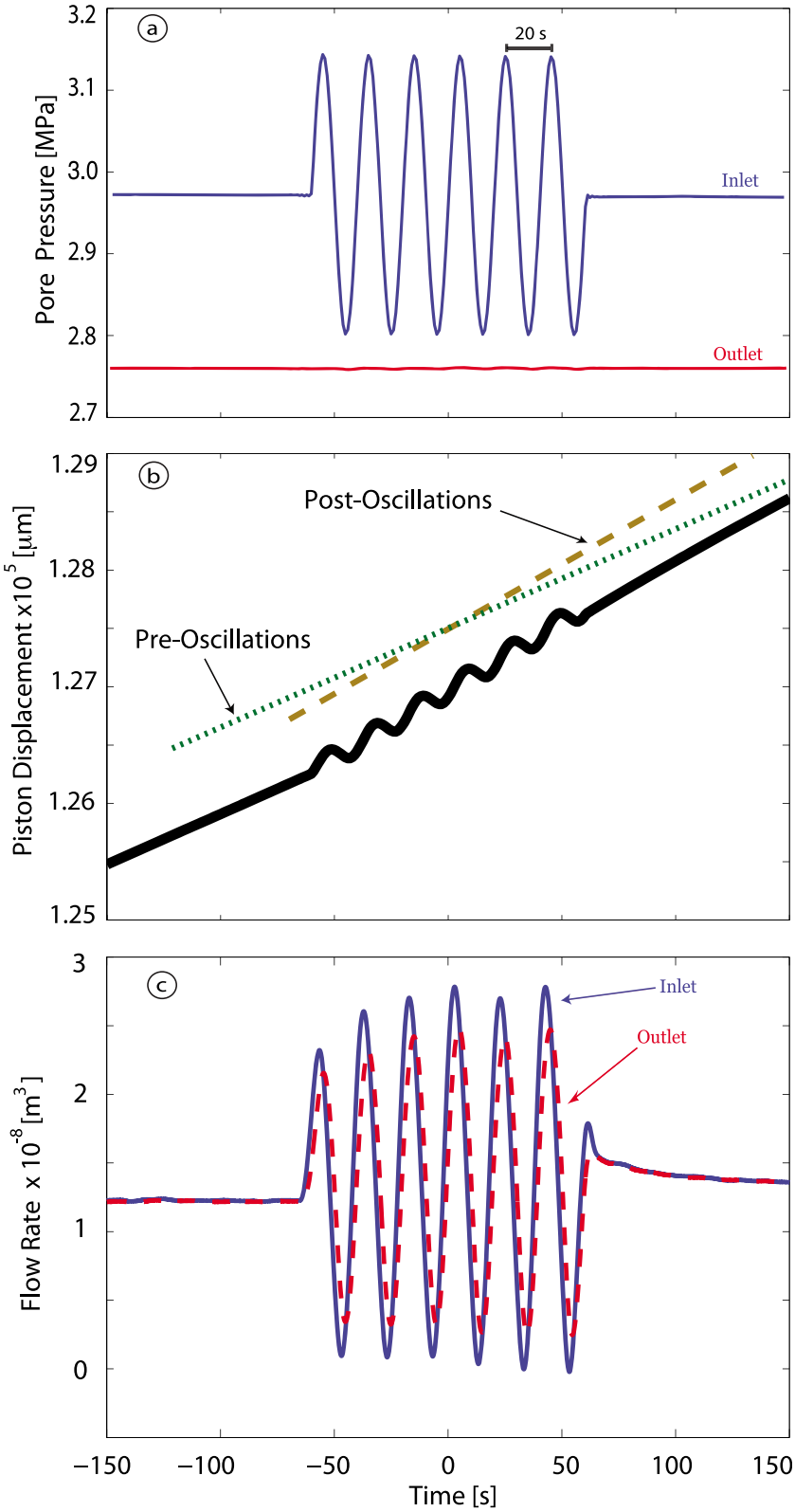
a
20 s
Pore Pressure [MPa]
3.2
3.1
3.0
2.9
2.8
2.7
Inlet
Outlet
b
Post-Oscillations
Pre-Oscillations
Piston Displacement x10^5 [µm]
1.29
1.28
1.27
1.26
1.25
c
Inlet
Outlet
Flow Rate x 10^-8 [m^3]
3
2
1
0
−150
−100
−50
0
50
100
150
Time [s]

Figure 6

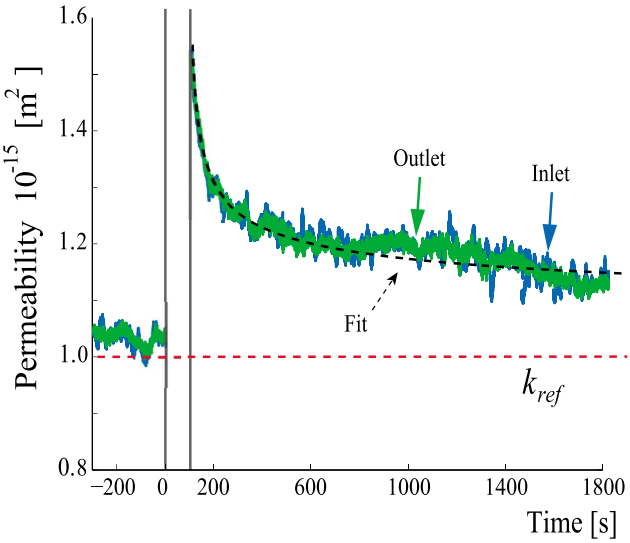

Figure 7. Effective permeability before and after the pore pressure oscillation shown in Figure 6. Note difference in time scale with Figure 6; the oscillation and the time immediately afterward are not included here. The effective permeability is directly proportional to the flow rate (Figure 6c) via equation (1). The two curves show the permeability measurements based on flow rates obtained independently by the movement of the inlet and outlet pistons. The striking overlap demonstrates that the interpretation of flow rate change as due to effective permeability change is accurate and the flow rate change is not related to storage or other poroelastic effects (see section 4.2). Permeability shows a step increase followed by a gradual recovery. A power law t^{-p} (dashed line) with exponent $p = 0.32$ fits the permeability recovery with a goodness of fit $R^2 = 0.96$. Here time $t = 0$ corresponds to the initiation of pore pressure oscillations. Horizontal red dashed line is the reference permeability k_{ref} defined as the permeability after fracture and shear but before the application of any pore pressure oscillations.

effect of amplitude, we kept the frequency and number of the oscillations constant for all of the experiments reported here. For this set of experiments we used a period of 20 s, which is representative of seismic waves. Future work should explore the effects of oscillation frequency and duration. We refer to each set of six oscillations as a single dynamic stress test, and each point in Figure 4 represents one such test.

[16] We measure the effective permeability of the fractured sample, which includes the matrix permeability of the unfractured sample. The effective permeability, k, is used as an interpretive tool to monitor the response of the fractured sample to the pressure oscillations. The fracture we produce, in situ, is a complex natural shear fracture containing a combination of mode II and mode I segments. While we do not observe the fluid flow path directly, comparison of the prefracture and postfracture sample (Figure 5) and the permeability data gives a good indication of the fracture flow and permeability. Moreover, after taking the samples out of the apparatus, we found gouge distributed over the fracture surface with more gouge in the downstream direction, indicating particle mobilization. We measure the effective permeability, k_a, by calculating the flow rate over a 2 s window (Figure 6). For pore pressure oscillations, we start 10 s after the oscillation to ensure that permeability measurement is not affected by the Pp oscillation and/or by storage effects.

[17] The detailed results presented here (Table 1) are a subset of experiments performed on 22 samples. These additional experiments are not part of our main data set but were important in developing the protocol for our experiments and thus merit a few comments. We explored the use of smooth artificial fractures produced between two rock surfaces that were prepared by cutting and grinding samples of Berea sandstone. Fracture surfaces were surface ground flat and then roughened with #60 grit SiC polishing compound. Fluid flow rates along these surfaces were very fast, and we were unable to observe reproducible permeability enhancement, even at the lowest ΔP values we could achieve (~50 kPa). A second set of tests considered natural shear fractures, as described in the primary suite of experiments, except that we applied flow rate boundary conditions at the inlet/outlet and measured the differential pore pressure. This approach was feasible but not optimal because of the finite fluid volume available from our pressure intensifiers (~125 cm^3; see *Samuelson et al.* [2009] and *Faoro et al.* [2009] for additional details). Additionally, we measured flow rates under step increases in pore pressure for which we did not observe measurable increases in permeability. Results of these additional tests were otherwise consistent with the main set of experiments, which we focus on here.

3. Results

[18] We present detailed results from experiments on four samples, which were each subjected to multiple sets of Pp oscillations (Table 1 and Figure 4). Between each set of oscillations, the sample was allowed to recover for 30 to 100 min (Figure 4). We report changes in permeability as $\Delta k = k_a - k_{ref}$, where k_a is effective permeability and k_{ref} is the initial, reference permeability after fracturing and shearing,

Figure 6. Example of dynamic stressing and the corresponding flow rate measurements for a set of pore pressure oscillations in experiment p1605. (a) Imposed pore pressure oscillations at inlet and fixed pore pressure at the outlet. Pressure conditions before and after the oscillations are identical. (b) Inlet fluid flow. Thick black line shows displacement of the piston in the upstream fluid pressure intensifier before, during, and after pressure oscillations. Green dotted line is parallel to preoscillations displacement, and the brown dashed line is parallel to postoscillation displacement. Piston displacement measures the volume of fluid that flows into the sample. The slope is flow rate after accounting for compressibility and specific storage. Note the clear increase in flow rate induced by the pressure oscillation as indicated by a higher slope of the dashed line compared with the dotted line. (c) Measured flow rates at the fracture inlet (blue line) and outlet (red dashed line). Notice the small time lag (≤2 s) between the maxima of the inlet and outlet flow rates. Here, time = 0 is an arbitrary reference that indicates the middle of the oscillation.

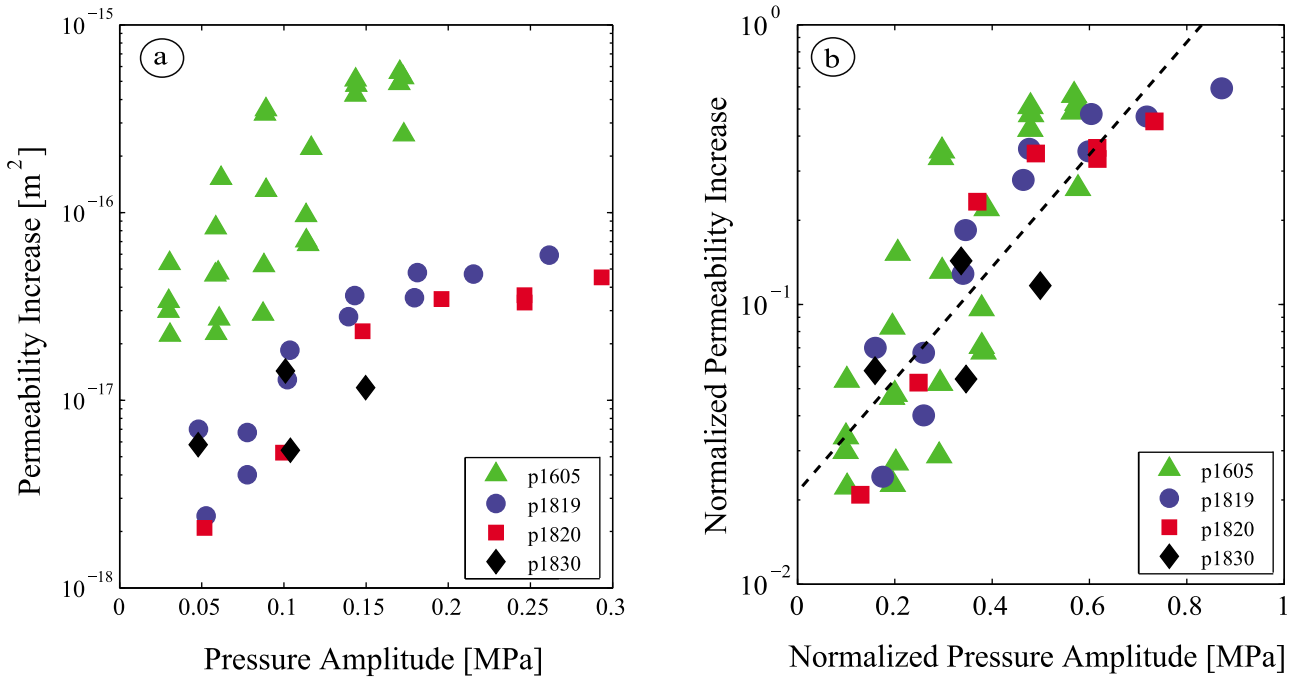

Figure 8. (a) Permeability increase, Δk, as a function of pore pressure oscillation amplitude. Oscillations were applied in sets of increasing amplitude (Figure 4). Permeability increases significantly as a function of oscillation amplitude. (b) Same data as in Figure 8a except permeability changes are normalized by k_{ref} and the pressure amplitudes are normalized by the pore pressure differential, ΔP, driving the flow. Data collapse onto one curve (dashed line is equation (2)). Note that permeability increases by nearly 2 orders of magnitude for our range of amplitudes.

but before pressure oscillations began (Figure 7). Table 1 provides details on the sample strength and fracture parameters, which gives a sense of reproducibility among the complex natural fractures. Table 1 also provides sample dimensions and values of the pore pressures used to assess permeability.

[19] We find that pore pressure oscillations produce transient increases in the flow rate (Figure 6). During the oscillations, we independently controlled the inlet and outlet pressures and monitored flow. Figure 6a details the *Pp* history for one set of oscillations. The mean value of ΔP before, during, and after oscillations is unchanged, and thus the average driving force for fluid flow remains constant. Figure 6b shows details of the flow rates before and after oscillations. The heavy black line shows the data. The slope of the green dotted line corresponds to preoscillations flow, and the slope of the brown dashed line corresponds to postoscillation flow. We note that the increase in flow rate is observed upon initiation of the pressure oscillations. Details of the flow rates measured at the inlet and outlet are shown in Figure 6c. These data indicate that flow through the fractured sample was rapid but small differences between inlet and outlet existed, with phase shifts of ~2 s and amplitude damping of up to 3×10^{-9} m^3/s in flow rate. Note that flow rates for the inlet and outlet track one another after the end of the *Pp* oscillations. Key observations include the following: (1) postoscillation flow rates exceed the preoscillation flow rates and (2) flow rate decays following the oscillation (Figure 6c). For each test, we found results like those presented in Figure 6.

[20] We calculated effective permeability of the fractured sample using the flow rates before and after *Pp* oscillations (Figure 7). These values represent effective permeability of the fractured sample, given that flow occurs within the fracture, in the damaged region around the fracture, and within the sandstone matrix. Our data consistently show that oscillatory forcing causes a step increase in permeability, followed by a gradual reduction to the preoscillation values (Figure 7). The decay of permeability toward its initial value follows a power law t^{-p}. Additional detail is provided below.

[21] For amplitudes of pore pressure oscillation in the range 0.02–0.3 MPa, the transient increases in permeability, $\Delta k = k_a - k_{ref}$, scale with amplitude (Figure 8). The absolute values of Δk increase are in the range 2×10^{-18} m^2 to 5×10^{-16} m^2 and vary slightly from sample to sample (Figure 8a), but the dependence on amplitude is consistent. To compare permeability changes between experiments quantitatively, we normalized changes by k_{ref}, the background permeability (Figure 8b). We also normalized the pore pressure amplitude, A, by the pore pressure differential, ΔP, driving the background flow. Figure 8b shows remarkable similarity between experiments, with all data falling on the same curve given by

$$\log\left(\frac{\Delta k}{k_{ref}}\right) = m\frac{A}{\Delta P} - f \qquad (2)$$

where the slope m is 2.1 with a 95% confidence interval given by the range 1.7 to 2.5, the constant f is 1.67 with a 95% confidence interval given by 1.5 to 1.8 and a goodness

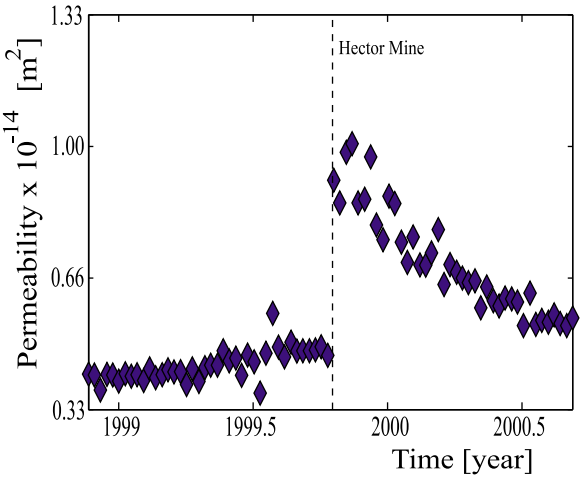

Figure 9. Permeability response to shaking at the Piñon Flat Observatory, in southern California, from the 1999 Hector Mine earthquake. Notice the clear qualitative similarity to Figure 7 (but differences in time scale). Permeability shows a step increase at the time of shaking (indicated by dashed line) with a gradual decrease over a time scale of months. In the lab, permeability recovery is achieved on the order of hours. (From *Elkhoury et al.* [2006].)

of fit measured by an $R^2 = 0.7$. Equation (2) is used because it is simple and consistent with the experimental data. However, it is only valid for the range of amplitudes in pore pressure oscillations considered in our experiments. We explore the permeability fit beyond the experimental conditions in section 4.3.

[22] Figure 8 demonstrates that effective permeability as defined by equation (1) is a well-defined quantity, despite details of the complex flow structure in the sample. The proof that the effective permeability is useful in a comparative sense is simply the reproducibility of the normalized permeability results of Figure 8. If our measure of permeability were poorly defined, then equation (2) would have no predictive power for the laboratory experiments, which is clearly not the case.

[23] To the best of our knowledge, the transient increases in permeability reported here provide the first consistent experimental evidence of flow enhancement by pore pressure oscillations. We observe step increases in permeability upon oscillatory forcing, followed by gradual recovery (Figure 7), akin to that observed in natural systems (Figure 9) [*Elkhoury et al.*, 2006]. Furthermore, the magnitude of our observed permeability enhancement increases systematically with increasing amplitude of the pore pressure oscillation (Figure 8).

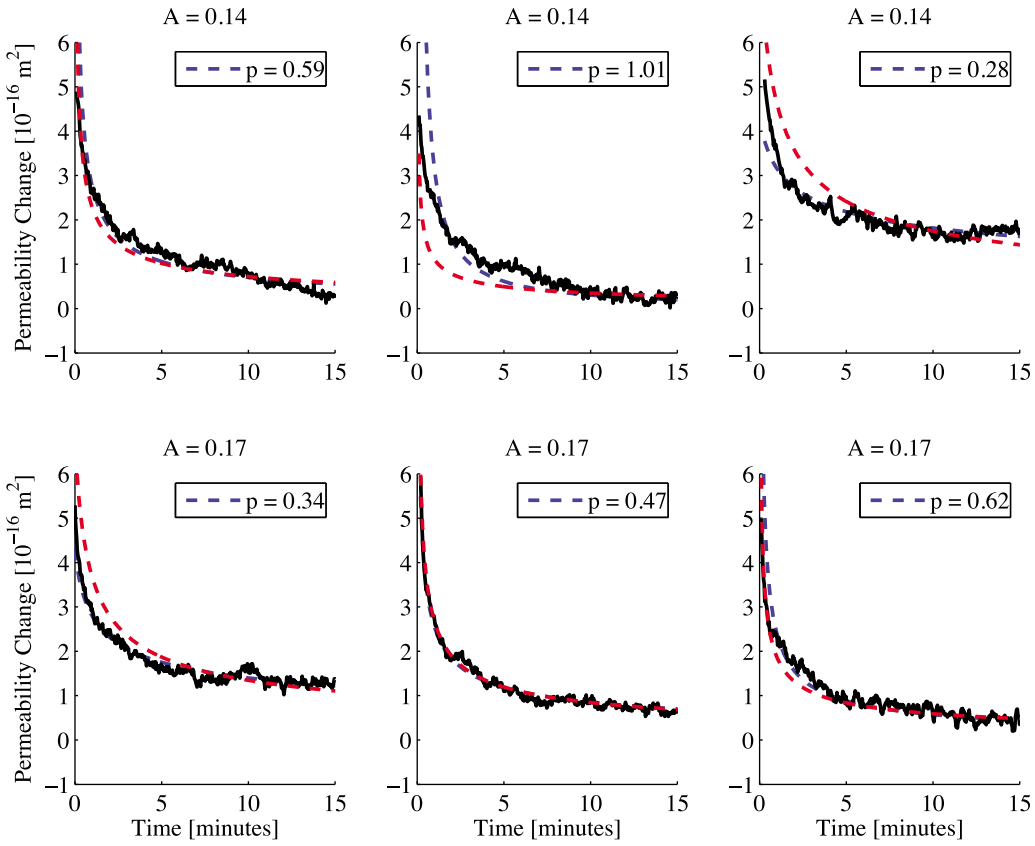

Figure 10. Recovery of permeability after fluid pressure oscillations for several sets of oscillations from experiment p1605 (black lines). Y axes are permeability changes, Δk, and X axes are time in minutes after the oscillation. Values of the amplitude of the oscillation, A, are in MPa. Dashed blue lines show power law fit t^{-p} with p values given in each plot. Note that p values range from 0.3 to 1.0. Red dashed lines show fits for $p = 0.5$; in this case, goodness of fit, R^2, ranges from 0.7 to 0.9.

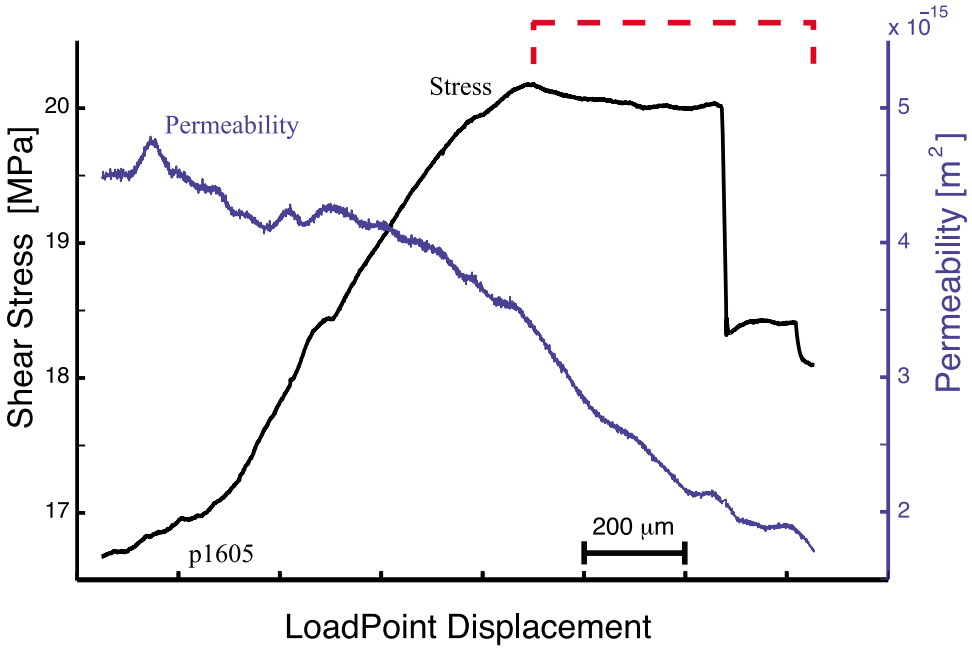

Figure 11. Permeability evolution as a function of shear displacement on the fracture (applied at the time of the vertical dashed line in Figure 4). Note that permeability drops from 4.4×10^{-15} m^2 to 1.1×10^{-15} m^2. The near vertical drop in stress represents an unstable, stick-slip event. Dashed bracket at top represents a net shear displacement of 600 μm along the fracture.

[24] The decay of permeability toward background levels, following oscillatory forcing is of interest. A power law fit of the form t^{-p} represents the recovery of permeability to preoscillation values (Figure 7). The exponent p ranges between 0.3 and 1.0 for our suite of experiments (Figure 10). Using $p = 0.5$ as a representative decay results in a slightly reduced, but still acceptable, goodness of fit (Figure 10). The square root dependence on time suggests a solution to a diffusion equation as would be expected for the migration of pore pressure that would be expected in a porous medium [e.g., *Bear*, 1979; I. Faoro et al., Permeability evolution during dynamic stressing of dual permeability media, submitted to *Journal of Geophysical Research*, 2010]. However, this permeability recovery is distinct from a poroelastic release of storage, as discussed in section 4.2.

[25] We probed the effect of fracture complexity and gouge development on transient permeability enhancement by progressively shearing the fracture after it was formed (Figure 11). Shear offset of the fracture decreased the effective permeability significantly, as indicated by the region marked by the dashed line in Figure 11. These data support the idea that most of the flow occurs within the fracture zone rather than in the sandstone matrix. In the other experiments, the samples were sheared immediately after fracturing, which further reduced permeability and therefore lowered the reference permeability.

4. Discussion

4.1. Potential Mechanisms of Permeability Enhancement

[26] The increase in effective permeability induced by oscillatory pore pressure can be explained by a number of potential mechanisms. We focus on (1) microfracturing and shear and (2) clogging/unclogging of fracture flow paths. In the first mechanism, the oscillation of the stress field due to the change in effective stress from the pore pressure oscillations results in (micro)failure of the solid material. These new cracks form an increased number of pathways for the flow and hence an effective permeability increase. In the second mechanism, pore pressure oscillations drive faster flow through existing fracture flow paths by removing transient barriers, such as rock powder generated by the fracturing process. Flow mobilizes the particulates and removes them from constrictions in the fracture network, resulting in unclogged fractures with larger effective permeability than prior to the oscillations. After dynamic stressing ceases, permeability of the system recovers due to clogging of the fracture mediated by settling of fine particles [*Bear*, 1979]. It is worth noting that the applied pressure oscillations are of very low frequencies compared to the critical frequency for which inertial terms dominates. Therefore, the dynamic effects observed are not controlled by the Navier-Stokes viscous terms [*Biot*, 1956] but rather correspond to effective permeability enhancement. Four observations favor the unclogging mechanism over microfracturing for our experiments: (1) recovery of the initial permeability after dynamic stressing, (2) the dependence of the permeability enhancement on the initial permeability of the sample, (3) a lack of permeability increase for unfractured, intact samples, and (4) a lack of observed normal stress oscillations and displacements normal to the fracture plane.

[27] As demonstrated in Figures 7 and 10, permeability returns to preoscillation values over a period of tens of minutes after dynamic stressing. This recovery requires a reversible mechanism, like unclogging of fractures, as

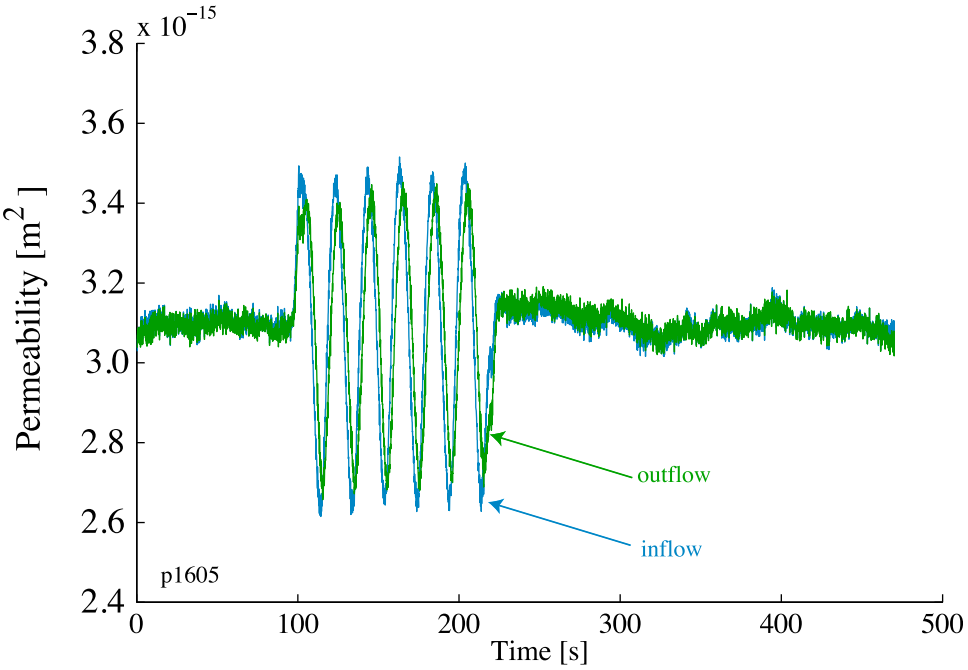

Figure 12. Effective permeability of the intact sample during pore pressure oscillations (as in Figure 6a). Permeability is determined from measured flow rates (see Figure 6b). Time zero is set arbitrarily to 100 s before the onset of oscillations. Note that permeability does not change following pressure oscillations; compare to Figures 6c and 7.

opposed to a permanent, irreversible change of the matrix properties, like microfacturing. If microfracturing were responsible for the permeability enhancement, then an additional mechanism of unusually rapid healing would be required to account for permeability recovery.

[28] The importance of the initial permeability, k_{ref}, in predicting the permeability changes is reflected in the collapse of all data onto the same curve (Figure 8b), which indicates a strong memory in the system. It implies that permeability enhancements after a given period of dynamic stressing are not affected by previous excitations, as would be expected for the formation of new pathways by microfracturing. Instead, the degree of permeability enhancement is controlled by a parameter that directly measures the propensity for flow, suggesting a role for fluid flow in directly controlling the subsequent structure.

[29] We also performed experiments on intact rock samples of Berea Sandstone (Figure 12) and Westerly Granite (no fracturing) in which we did not observe changes in permeability under the influence of pore pressure oscillations. This points to the importance of fine particles along the flow path and the heterogeneity of the natural fracture in controlling the flow and subsequent response to dynamic stressing. Microfracturing would have been expected to be effective in the intact samples.

[30] The effective permeability enhancements are not affected by fluctuations in the effective normal stress. The amplitude of the pore pressure oscillations was ~0.2 MPa over a fixed background effective stress of 20 MPa. Therefore, variations in effective normal stress are ~1% of the total effective normal stress. Moreover, we impose the dynamic stressing through pore pressure oscillations around a constant preoscillation pore pressure value. Hence, the average effective normal stress during the oscillations is the same as the background stress. This lack of normal stress oscillations in the solid matrix makes failure through microfracturing unlikely [*Townend and Zoback*, 2000; *Nemoto et al.*, 2009].

[31] Taken together, our observations strongly favor clogging/unclogging as the potential mechanism for transient changes in permeability. However, there is one potentially conflicting observation. If particle mobilization is controlling permeability, either clogging or unclogging of fracture throats should be possible. Therefore, we could potentially observe either permeability increases or decreases. For our full suite of experiments, only one occasion of dynamic stressing in 50 produced a transient decrease in permeability. The sign of shaking-induced permeability changes could vary with rock properties and fracture characteristics. Additional work to explore this aspect of the experiment will require significant technical enhancements to the experimental setting to directly monitor particulate flow and is beyond the scope of this paper.

[32] On the basis of the current evidence, we conclude that unclogging is the mechanism that best explains our experimental observations of permeability increase by pore pressure oscillations. We note that our experiments are necessarily limited to measuring effective permeability across the bulk sample and thus direct probing of the location of the fracture permeability is not possible. However, unclogging is consistent with a larger number of the observations than the alternative mechanism of microfracturing.

4.2. Poroelastic Contribution of Storage

[33] Apparent changes of permeability could be produced by transient storage in the sample. In principle, a release of

fluid trapped within the sample could mimic an effective permeability increase. However, in our experiments, storage effects were small as indicated by comparison of the input and output flow (Figures 6 and 7). Given the importance of this point, we now evaluate the contribution from such poroelastic effects and quantitatively demonstrate that they are not controlling the inferred effective permeability increases. We calculate the volume of fluid released from storage in the sample during and after an applied pore pressure oscillation based on the measured poroelastic properties and compare it to the volume of fluid involved in the inferred effective permeability increase.

[34] In order to measure the specific storage of the sample, we first calculate the hydraulic diffusivity based on the observed time lag of the outlet flow relative to the inlet flow. The average time delay, ΔT, between maxima in the inlet and outlet flow rates during pressure oscillations is 2 s (Figure 6c). Given the flow path length scale, $L = 2\sqrt{\nu\ \Delta T}$, of 49.4 mm (for the case of experiment p1605), we obtain diffusivity $\nu = 3.05 \times 10^{-4}$ m^2/s for the fractured sample. The specific storage, S_s, defined as [*Wang*, 2000]

$$S_s = \frac{k}{\mu\ \nu} \tag{3}$$

is $S_s = 3.28 \times 10^{-9}$ Pa^{-1}, for a permeability, k, of 10^{-15} m^2 (Figure 7).

[35] We verify this poroelastic specific storage value by checking the inferred volume release during the experiment (Figure 6) with the direct measurements of fluid flow. For this example, the amplitude of the pore pressure oscillation is 0.3 MPa (Table 1). Therefore, the fraction of stored volume is $S_s = 3.28 \times 10^{-9}$ Pa^{-1} $\times$ 3.00×10^5 Pa = 9.83×10^{-4}. Given the sample volume of 6.05×10^{-5} m^3, the resulting inferred volume released is 5.95×10^{-8} m^3. This inference is consistent with direct measurements of the total volume difference of 5.18×10^{-8} m^3 between the inlet and outlet fluid volume. On the other hand, the integrated volume of fluid during 15 min of permeability recovery, immediately after the cessation of the pore pressure oscillation, at the inlet and outlet is 7.04×10^{-6} m^3. This volume is orders of magnitude higher than the storage volume released and cannot be accounted for by poroelastic effects. Moreover, the poroelastic response is dissipated within the first 4 s after the culmination of the dynamic stressing. This is well within the window (10 s) that we omitted from the analysis (Figures 6 and 7).

4.3. Permeability Recovery

[36] Because we are interested in the permeability response to pore pressure oscillations, we focus on values of permeability before and after oscillations (Figure 7); however, the experiments contain additional information. Figure 10 shows the permeability recovery after dynamic stressing for two sets of pore pressure oscillations in one experiment. These data allow evaluation of the natural variability in peak permeability enhancement and in recovery among the repeat tests conducted in each experiment. Although there is some variability, the data are generally consistent with power law exponents ranging from 0.3 to 1. A fixed exponent p of 0.5 is a reasonable overall fit to each of the pore pressure oscillations tests (Figure 10). The exponent p could be related to the fractal flow dimension of the fracture, which can vary from oscillation to oscillation [*Walker and Roberts*, 2003]. Therefore, p can be interpreted as the inverse of the dimension, d, of the system, $p \sim 1/d$. Since our samples develop two-dimensional shear fractures, the average flow dimension is $d = 2$. Hence, $p \sim 0.5$ appears to be a good average exponent value to represent the overall recovery of the permeability as suggested previously by *Bear* [1979] and *Barker* [1988].

4.4. Flow-Driven Permeability Enhancements

[37] Our data indicate an exponential relationship between permeability enhancements (equation (2)) and the amplitude of the applied pore pressure oscillation. The exponential relationship means that permeability increase is proportional to the preexisting permeability for the fractured samples. The easier it is for water to flow through the fractured sample, the greater the permeability increase. This dependency suggests that the mechanism for permeability enhancement may be water flowing through and opening up the fractures. For instance, if the flow is removing fine particles in the fracture and thus opening up new pathways (or widening pathways), we might expect that the cross-sectional area of the fracture cleaned would be proportional to the ratio of the excess flow rate over the background flow. In this case, the effective permeability increase would also be proportional to the excess flow and thus

$$\mathrm{d}k_f \propto u_f \tag{4}$$

where k_f is the permeability in the fracture and u_f is the excess flow in the fracture. According to Darcy's law, for a fixed path length,

$$u_f \propto k_f A \tag{5}$$

where A is the amplitude of the imposed pressure oscillation. Combining equations (4) with (2) and integrating results in

$$\ln\left(k_f\right) \propto A \tag{6}$$

as observed. The consistency means that a flow-driven mechanism for permeability enhancements is concordant with a flow rate threshold for permeability enhancement. Micromechanically, this flow rate threshold could be generated through mobilization of fine particles.

4.5. Permeability Fit Beyond the Experimental Conditions

[38] The fit of equation (2) used in Figure 8b was restricted to a logarithmic relationship. However, it is only valid for the range of amplitudes in pore pressure oscillations explored. In particular, the relationship is problematic for very small amplitudes. If $A = 0$, equation (2) has the unphysical behavior that $\Delta k/k_{ref}$ is finite; that is, there is a permeability increase in the absence of any oscillations. To remedy this problem and to extend the correlation beyond the experimental range, we suggest an equivalent relation of the form

$$\frac{\Delta k}{k_{ref}} = a\left(\frac{A}{\Delta P}\right)^b \tag{7}$$

where $a = 0.7$ and $b = 1.7$ are fitting constants and goodness of fit given by an $R^2 = 0.88$.

[39] The opposite limit of a larger value of A relative to ΔP is more problematic. In their present simplified form, neither equation (2) nor equation (7) extrapolates successfully to the field data of *Elkhoury et al.* [2006]. The field observations of perturbations to the tidally driven flow by seismic waves record a system in which both the imposed oscillations and background stresses are proportional to imposed dilatational strains. The strain in the seismic waves is on the order of 10^{-5}. The tidally driven flow into an open well has a peak pressure difference (ΔP) proportional to the peak dilatational strain of 10^{-8}. Therefore, for the water well observations, $A/\Delta P = 10^3$. In contrast, $A/\Delta P = 10^{-1}$ for the experiments presented here. An extrapolation of equation (7) to the field observations predicts $k/k_{ref} \approx 1000$ rather than $k/k_{ref} = 3$ or 4 as observed [*Elkhoury et al.*, 2006]. Extrapolation of the laboratory data to the field scale is not straightforward.

[40] One possible explanation for the discrepancy is that the ΔP dependence is incompletely captured by the current experiments as the current work explored a range of values of A, not ΔP. Another alternative is introduced by the fact that the field system is clearly more complex than the small-scale laboratory samples. The multiple fractures and highly heterogeneous matrix likely have a different composite behavior than that of a single fracture, and the scale of the imposed tidal strain is not the same as the higher-frequency seismic waves [*Doan et al.*, 2007]. For now, we note that either equation (2) or (7) successfully explains laboratory data showing permeability enhancement by dynamic stressing.

5. Conclusions and Implications

[41] We observe systematic increases in effective permeability due to dynamic stressing produced by pore pressure oscillations. We used relatively small peak pressures (10^{-2} to 10^{-1} MPa) and found effective permeability changes of up to 50% in a fracture-dominated system. Our results show that (1) effective permeability of fractured laboratory samples can be reliably and reproducibly increased by fluid pressure oscillations, (2) accurate prediction of the effective permeability changes requires normalization by the initial permeability of the system, indicating a memory of the initial state of the system, and (3) oscillating the pore pressure results in a logarithmic enhancement, under the experimental conditions considered, which is consistent with a flow-driven mechanism. Mobilization of fine particles and associated clogging/unclogging of the fracture flow path appear to explain most of our laboratory observations.

[42] Our result has consequences for a range of problems encountered in hydrology and oil reservoir engineering and in geophysics, where earthquake triggering may be mediated by permeability enhancement in fault zones due to shaking from near and distant earthquakes. In particular, observations of delayed dynamic earthquake triggering can be tied to fluid-mediated processes initiated at the time of the passage of seismic waves that enhance the permeability of the triggered fault system. *Brodsky et al.* [2003] and *Brodsky and Prejean* [2005] suggested that such permeability enhancements were responsible for dynamic triggering. The seismic waves were thought to break seals between hydrologic compartments in the fault zone, and the resulting pressure reequilibration would induce seismicity through effective stress changes. Our experiments show that at least one stage of this process, i.e., the permeability change from seismic waves, is plausible.

[43] The permeability increases and decreases we report are related to mechanical processes rather than mechanisms of irreversible, long-term thermally activated healing and sealing processes. Thus, our results represent additional, complimentary processes to those discussed by works on fault healing and sealing, [e.g., *Brantley et al.*, 1990; *Blanpied et al.*, 1992; *Karner et al.*, 1997; *Olsen et al.*, 1998; *Tenthorey et al.*, 2003; *Tenthorey and Cox*, 2006; *Niemeijer et al.*, 2008]. Our results suggest that gouge creation during earthquake fracture reduces the fault permeability and therefore increases pore pressure in the fault zone.

[44] The effects of dynamic stressing also suggest that permeability is a dynamically controlled variable. The sensitivity of fractured systems to shaking illustrated here implies that permeability is expected to vary over time due to regional seismicity. Therefore, competing processes may be responsible for a return to an average value. Such dynamic control is required to explain the long-term stability of the baseline permeability observed by *Elkhoury et al.* [2006].

[45] Our experiments imply that dynamically controlling permeability of fractured systems is feasible. We cautiously suggest that artificial stimulation in reservoir systems can mimic the behavior observed in the lab and therefore enhance production. Clearly the engineering challenges to such an application are formidable, but the demonstration of a reproducible laboratory effect is one of the first steps toward defining an operational procedure.

[46] **Acknowledgments.** We gratefully acknowledge experimental support by I. Faoro and J. Samuelson and comments from H. Kanamori and D. Elsworth. This work was supported in part by NSF grants OCE-0648331 and EAR-0545702. A.R.N. was supported by NWO (Dutch Science Foundation) grant 825.06.003.

References

Barker, J. A. (1988), A generalized radial flow model for hydraulic tests in fractured rock, *Water Resour. Res.*, *24*(10), 1796–1804, doi:10.1029/WR024i010p01796.

Bear, J. (1979), *Hydraulics of Groundwater*, McGraw-Hill, London.

Beresnev, I. A., and P. A. Johnson (1994), Elastic-wave stimulation of oil production: A review of methods and results, *Geophysics*, *59*, 1000–1017, doi:10.1190/1.1443645.

Biot, M. A. (1956), Theory of deformation of a porous viscoelastic anisotropic solid, *J. Appl. Phys.*, *27*, 459–467, doi:10.1063/1.1722402.

Blanpied, M. L., D. A. Lockner, and J. D. Byerlee (1992), An earthquake mechanism based on rapid sealing of faults, *Nature*, *358*, 574–576, doi:10.1038/358574a0.

Brantley, S. L., B. Evans, S. H. Hickman, and D. A. Crera (1990), Healing of microcracks in quartz—Implications for fluid-flow, *Geology*, *18*, 136–139, doi:10.1130/0091-7613(1990)018<0136:HOMIQI>2.3.CO;2.

Brodsky, E. E., and S. G. Prejean (2005), New constraints on mechanisms of remotely triggered seismicity at Long Valley Caldera, *J. Geophys. Res.*, *110*, B04302, doi:10.1029/2004JB003211.

Brodsky, E. E., E. Roeloffs, D. Woodcock, I. Gall, and M. Manga (2003), A mechanism for sustained groundwater pressure changes induced by distant earthquakes, *J. Geophys. Res.*, *108*(B8), 2390, doi:10.1029/2002JB002321.

Coble, R. W. (1965), The effects of the Alaskan earthquake of March 27, 1964, on ground water in Iowa, *Proc. Iowa Acad. Sci.*, *72*, 323–332.

Doan, M., E. E. Brodsky, and D. C. Agnew (2007), Mechanisms of permeability enhancement by seismic waves at Piñon Flat Observatory, *Eos Trans. AGU*, *88*(52), Fall Meet. Suppl., Abstract H11B-0481.

Elkhoury, J. E., E. E. Brodsky, and D. C. Agnew (2006), Seismic waves increase permeability, *Nature*, *441*(7097), 1135–1138, doi:10.1038/nature04798.

Faoro, I., A. Niemeijer, C. Marone, and D. Elsworth (2009), The influence of shear and deviatoric stress on the evolution of permeability in fractured rock, *J. Geophys. Res.*, *114*, B01201, doi:10.1029/2007JB005372.

Felzer, K. R., and E. E. Brodsky (2006), Decay of aftershock density with distance indicates triggering by dynamic stress, *Nature*, *441*(7094), 735–738, doi:10.1038/nature04799.

Gomberg, J., J. L. Rubinstein, Z. G. Peng, K. C. Creager, J. Vidale, and P. Bodin (2008), Widespread triggering of nonvolcanic tremor in California, *Science*, *319*(5860), 173, doi:10.1126/science.1149164.

Hill, D. P., et al. (1993), Seismicity remotely triggered by the magnitude 7.3 Landers, California, earthquake, *Science*, *260*(5114), 1617–1623, doi:10.1126/science.260.5114.1617.

Ikari, M., D. M. Saffer, and C. Marone (2009), Frictional and hydrologic properties of clay-rich fault gouge, *J. Geophys. Res.*, *114*, B05409, doi:10.1029/2008JB006089.

Karner, S. L., C. Marone, and B. Evans (1997), Laboratory study of fault healing and lithification in simulated fault gouge under hydrothermal conditions, *Tectonophysics*, *277*, 41–55, doi:10.1016/S0040-1951(97)00077-2.

Main, I. G., O. Kwon, B. T. Ngwenya, and S. C. Elphick (2000), Fault sealing during deformation-band growth in porous sandstone, *Geology*, *28*, 1131–1134, doi:10.1130/0091-7613(2000)28<1131:FSDDGI>2.0.CO;2.

Manga, M., and E. E. Brodsky (2006), Seismic triggering of eruptions in the far field: Volcanoes and geysers, *Annu. Rev. Earth Planet. Sci.*, *34*, 263–291, doi:10.1146/annurev.earth.34.031405.125125.

Manga, M., and C. Y. Wang (2007), Earthquake hydrology, in *Treatise on Geophysics*, vol. 4, *Earthquake Seismology*, edited by H. Kanamori, pp. 293–320, Elsevier, Boston, Mass.

Manga, M., E. E. Brodsky, and M. Boone (2003), Response of stream flow to multiple earthquakes, *Geophys. Res. Lett.*, *30*(5), 1214, doi:10.1029/2002GL016618.

Muir-Wood, R., and G. C. P. King (1993), Hydrological signatures of earthquake strain, *J. Geophys. Res.*, *98*, 22,035–22,068, doi:10.1029/93JB02219.

Nemoto, K., N. Watanabe, N. Hirano, and N. Tsuchiya (2009), Direct measurement of contact area and stress dependence of anisotropic flow through rock fracture with heterogeneous aperture distribution, *Earth Planet. Sci. Lett.*, *281*, 81–87, doi:10.1016/j.epsl.2009.02.005.

Niemeijer, A., C. Marone, and D. Elsworth (2008), Healing of simulated fault gouges aided by pressure solution: Results from rock analogue experiments, *J. Geophys. Res.*, *113*, B04204, doi:10.1029/2007JB005376.

Olsen, M. P., C. H. Scholz, and A. Léger (1998), Healing and sealing of a simulated fault gouge under hydrothermal conditions: Implications for fault healing, *J. Geophys. Res.*, *103*, 7421–7430, doi:10.1029/97JB03402.

Roberts, P., I. B. Esipov, and E. L. Majer (2003), Elastic wave stimulation of oil reservoirs: Promising EOR technology?, *Leading Edge*, *22*(5), 448–453, doi:10.1190/1.1579578.

Rojstaczer, S., and S. Wolf (1992), Permeability changes associated with large earthquakes: An example from Loma Prieta, California, *Geology*, *20*, 211–214.

Rubinstein, J. L., J. E. Vidale, J. Gomberg, P. Bodin, K. C. Creager, and S. Malon (2007), Non-volcanic tremor driven by large transient shear stresses, *Nature*, *448*, 579–582, doi:10.1038/nature06017.

Samuelson, J., D. Elsworth, and C. Marone (2009), Shear-induced dilatancy of fluid-saturated faults: Experiment and theory, *J. Geophys. Res.*, *114*, B12404, doi:10.1029/2008JB006273.

Shelly, D. R. (2010), Migrating tremors illuminate complex deformation beneath the seismogenic San Andreas Fault, *Nature*, *463*(7281), 648–652, doi:10.1038/nature08755.

Tenthorey, E., and S. F. Cox (2006), Cohesive strengthening of fault zones during the interseismic period: An experimental study, *J. Geophys. Res.*, *111*, B09202, doi:10.1029/2005JB004122.

Tenthorey, E., S. F. Cox, and H. F. Todd (2003), Evolution of strength recovery and permeability during fluid-rock reaction in experimental fault zones, *Earth Planet. Sci. Lett.*, *206*, 161–172, doi:10.1016/S0012-821X(02)01082-8.

Townend, J., and M. D. Zoback (2000), How faulting keeps the crust strong, *Geology*, *28*(5), 399–402, doi:10.1130/0091-7613(2000)28<399:HFKTCS>2.0.CO;2.

Walker, D. D., and R. M. Roberts (2003), Flow dimensions corresponding to hydrogeologic conditions, *Water Resour. Res.*, *39*(12), 1349, doi:10.1029/2002WR001511.

Wang, H. (2000), *Theory of Linear Poroelasticity*, Princeton Univ. Press, Princeton, N. J.

E. E. Brodsky, Department of Earth and Planetary Sciences, University of California, Santa Cruz, CA 95060, USA.

J. E. Elkhoury, Seismological Laboratory, California Institute of Technology, 1200 E. California Blvd., Pasadena, CA 91125-0000, USA. (elkhoury@caltech.edu)

C. Marone, Department of Geosciences, Pennsylvania State University, 536 Deike Bldg., University Park, PA 16802, USA.

A. Niemeijer, Istituto Nazionale di Geofisica e Vulcanologia, Via di Vigna Murata, 605, I-00143 Roma, Italy.